Revista Brasileira de Engenharia Biomédica,
v. 26, n. 3, p. 219-233, dezembro 2010

ISSN 1517-3151
http://dx.doi.org/10.4322/rbeb.2012.089

Artigo Original
Recebido em 08/03/2009, aceito em 21/09/2010

An approach to automatically segment the media-adventitia borders in IVUS

Uma associação de técnicas para segmentação automática da fronteira da média-adventícia em IVUS

Matheus Cardoso Moraes*
Sérgio Shiguemi Furuie
Laboratório de Engenharia Biomédica,
Departamento de Engenharia de Telecomunicações e Controle - Escola Politécnica / USP
Av. Prof. Luciano Gualberto, Travessa 3, 158 - sala D2-06, 05508-970 São Paulo, SP – Brazil
E-mail: matheuscardosomg@hotmail.com

* Corresponding author

Abstract
By being able to show morphological and pathological aspects of atherosclerosis, the Intravascular Ultrasound (IVUS) became one of the most reliable and employed medical imaging modality in cardiac interventions. Its image characteristics increase the chances of a good diagnostic, resulting in a precise therapy. The study of media-adventitia borders segmentation in IVUS, among many applications, is important for learning about the mechanical properties and determining some specific measurements (radius, diameter, etc.) in vases and plaques. An approach is proposed to achieve high accuracy in media-adventitia borders segmentation, by making a combination of different image processing operations: Speckle Reducing Anisotropic Diffusion (SRAD), Wavelet, Otsu and Mathematical Morphology. Firstly, SRAD is applied to attenuate the speckle noise. Next, the vessel and plaque features are extracted by performing Wavelet Transform. Optimal thresholding is carried out by Otsu method to create a binarized version of these features. Then, Mathematical Morphology operations are used to obtain an adventitia shape. The proposed approach is evaluated by segmenting 100 challenging images, obtaining an average of True Positive (TP(%)) = 92.83 ± 4.91, False Positive (FP(%)) = 3.43 ± 3.47, False Negative (FN(%)) = 7.17 ± 4.91, Max False Positive (Max_{FP}(mm)) = 0.27 ± 0.22, Max False Negative (Max_{FN}(mm)) = 0.31 ± 0.2. The effectiveness of our approach is demonstrated by comparing this result with another recent work in the literature.

Keywords: Intravascular ultrasound (IVUS), Adventitia segmentation, Speckle Reducing Anisotropic Diffusion (SRAD), Discrete Wavelet Packet Frame (DWPF), Otsu, Mathematical morphology.

Resumo
Por ser capaz de mostrar aspectos morfológicos e patológicos de ateroscleroses, o Ultrassom Intravascular (IVUS) se tornou uma das modalidades de imagens médicas mais confiáveis e empregadas em intervenções cardíacas. As características de sua imagem aumentam as chances de um bom diagnóstico, resultando em terapias mais precisas. O estudo de segmentação da fronteira média-adventícia, dentre muitas aplicações, é importante para o aprendizado das propriedades mecânicas e determinação de algumas medidas específicas (raio, diâmetro, etc.) em vasos e placas. Neste trabalho, uma associação de técnicas de processamento de imagens está sendo proposta para atingir alta acurácia na segmentação da borda média-adventícia. Para tanto, foi feita uma combinação das seguintes técnicas: Redução do Speckle por Difusão Anisotrópica (SRAD), Wavelet, Otsu e Morfologia Matemática. Primeiramente, é usado SRAD para atenuar os ruídos speckle. Posteriormente, é executada Transformada Wavelet para extração das características dos vasos e placas. Uma versão binarizada dessas características é criada na qual o limiar ótimo é definido por Otsu. Finalmente, é usada Morfologia Matemática para obtenção do formato da adventícia. O método proposto é avaliado ao segmentar 100 imagens de alta complexidade, obtendo uma média de Verdadeiro Positivo (TP(%)) = 92,83 ± 4,91, Falso Positivo (FP(%)) = 3,43 ± 3,47, Falso Negativo (FN(%)) = 7,17 ± 4,91, Máximo Falso Positivo (Max_{FP}(mm)) = 0,27 ± 0,22, Máximo Falso Negativo (Max_{FN}(mm)) = 0,31 ± 0,2. A eficácia do nosso método é demonstrada, comparando este resultado com outro trabalho recente na literatura.

Palavras-chave: *Ultrassom intravascular (IVUS), Segmentação da adventícia, Redução do Speckle por Difusão Anisotrópica (SRAD), Quadros de Pacotes Wavelets Discretos (DWPF), Otsu, Morfologia matemática.*

Introduction

Atherosclerosis

Atherosclerosis is the accumulation of plaques in vessel's walls. The plaques are composed by different levels of three kinds of tissue (lipidic, fibrous and calcified). It may cause vessel occlusion, and thus decrease or even block blood irrigation at the affected areas. Depending on where it takes place and on what the predominant tissue is, the consequences can be fatal, resulting in thromboses, stroke, and in the coronary, it can culminate in a heart attack or sudden cardiac death (Barajas *et al*., 2007). The lipidic tissues pose the highest risks; on the other hand, if most of the tissues are fibrotic or calcified, they pose low risk and are usually well treated with stents.

More than 250,000 lives are taken annually in United States by atherosclerotic plaques, being the major reason of fatal acute coronary events (Katouzian *et al*., 2008a). Therefore, in order to lead to more precise diagnostics and therapy, it is extremely important to understand the mechanism of plaques behavior and supply health professionals with more adequate analysis tools.

Intravascular ultrasound (IVUS)

IVUS is a medical imaging modality which provides morphologic as well as some pathologic information about the occluded plaques throughout the coronary arteries. It is not only widely employed in the cardiac interventional procedures, but it is also known to be the reference tool for preoperative vessel lesion assessments and for endovascular therapy planning (Katouzian *et al*., 2008b; Maurice *et al*., 2004).

The advantage of using IVUS instead of angiography is that the former not only allows health professionals to see and measure the lumen, but it also shows the structure of the arterial wall and atherosclerotic plaques, making it easy to analyze the size of lesions and infer about their composition.

The images are acquired by inserting a specific catheter inside the coronary. It contains a miniaturized ultrasound transducer at one extremity with computerized ultrasound equipment at the other. The sequences of images correspond to cross sections along the coronary, which are acquired during the pull back movement with a selected sample rate and resolution (Reiber *et al*., 2000). Specifically, the acquisitions were performed by a Vulcano VH computerized ultrasound equipment, 64 arrays of transducers, 20 MHz, 10 frames per second, and pullback speed of 0.5 mm/s.

Segmentation

Segmentation is the process of recognizing and separating the image into regions related to a specific object; it defines contours that highlight the wanted object from the others (Dawant and Zijdenbos, 2000; Nyúl *et al*., 2003). Some applications concerning IVUS segmentation are: studies of vessel and plaque characteristics, mechanical properties, anatomical structures, tissue qualification and volume quantification, lumen and elastic-lamina size and radius, therapy plans and evaluations, localization of pathologies, 3D reconstruction (Nyúl *et al*., 2003; Unal *et al*., 2008; Xu *et al*., 2000). Direct or indirectly, segmentation is used in most of the image processing applications, and it is known as one of the most important and difficult image operation steps (Nyúl *et al*., 2003; Udupa *et al*., 2006; Udupa and Samarasekera, 1996).

According to Lobregt and Viergever (1995), segmentation can be performed in 4 different ways: a) Completely manual, in which a high skilled operator, using appropriate tools conduct the image segmentation; the authors emphasize that it is a hard and time consuming task, with bottlenecks for 3D images; b) Semi-automatic initialized with seed; c) Semi-automatic initialized with approximate contour; these two latter ways of segmentations have limited operator's interaction, yet it does not exempt him or her of having determined knowledge; d) Completely automatic, the fully automatic segmentation algorithms do not need the operator to give any direction, but the great variability of the object format and image quality makes the medical-imaging fully automated segmentation a great challenge for creating the appropriate algorithms (Nyúl *et al*., 2003; Xu *et al*., 2000). As the autonomous system is an increasing tendency, the fully automatic approach will be investigated here.

The state of the art

Recently many relevant segmentation works, using different techniques, have been proposed in the literature. Nyúl *et al*. (2003), Pednekar and Kakadiaris (2006), and Udupa and Samarasekera (1996) apply the concepts of fuzzy connectedness. The theory of deformable contours, such as snakes, can be found in Chan and Vese (2001), Lobregt and Viergever (1995), and Xu and Prince (1998). Katouzian *et al*. (2008b) and Unal *et al*. (2008) are specifically applied in IVUS.

The first (Katouzian *et al*., 2008b) combine the Discrete Wavelet Packet Frame (DWPF) (Coifman and Wickerhauser, 1992), the algorithm k-means clustering, and the spline interpolation to segment the lumen

in IVUS images. The algorithm works as follows. First, the DWPF is performed so as to extract the features related to the blood regions. Second, the features extracted are used as attributes so that the k-means can classify the texture related to the blood regions. Finally, the k-mean clusters that most represent the blood border (lumen border) were used as reference for the spline interpolation. The algorithm is evaluated by segmenting and computing the Tanimoto coefficient for a set of *in vivo* and *in vitro* IVUS images. The long time to compute the k-mean clusters for the correspondent image features, derived from the DWPF, can be considered the major disadvantage of this method.

In Unal *et al*. (2008) the authors present a lumen and vessel wall (elastic lamina – media adventitia border) segmentation technique. The method is divided into two parts. The first is the training part, where a set of shapes for the lumen and media-adventitia border are built in the polar domain using a set of training images and Principal Components Analysis (PCA). After constructing this set of forms, the segmentation process works as follows. In polar domain and using as a reference the catheter reflection, an initial contour is created automatically. As some others, this also uses an energy minimization process to evolve the contour; in addition to that, the Probability Density Function (PDF) from inside and outside the contour is considered in the minimization energy formula. The PDFs are obtained by Parzen windowing during the training part, and they are respectively associated to the internal and external forces in the energy formula. The algorithm has a special block (Feature Detection) to detect and correct side branches. In order to evaluate their method, the authors used two sets of images. The first set contained images with minor calcification and branch opening, and no feature detection was tested. The second set of images incorporated the images from the first test and also included some more challenging ones, with large calcification and branch opening. Their outcomes were corroborated after segmenting the lumen and adventitia from these two sets of images, and computing with high level of accuracy the following index: Overlap Ratio (OR) [OR=TP/(TP+FN+FP)]; False Positive Rate (FPR) [FPR=FP/(FP+TN)]; False Negative Rate (FNR) [FNR=FN/(FN+TP)], as well as the Mean Distance, Maximum Distance and Area. The main drawback of this method is the need of training and computation of huge eigenvectors.

Objective

Since the above works use really heavy operations (PCA and k-means) for imaging processing, the main goal of this work is to use a lighter set of imaging processing techniques, which combine a sequence of morphological operations so as to create an unsupervised, reliable and simple segmentation method able to automatically detect the contour of the vessel's elastic lamina (media-adventitia border) in IVUS image.

Materials and Methods

The material used in this work consists of a challenging set of IVUS images with mixed features such as images with small and large plaques, including calcification, as well as branch opening. We used 100 IVUS images from 24 different patients. The images were from the database of the Heart Institute of São Paulo, Brazil (InCor). The patients have written an informed consent, and the study protocol has been approved by the local ethics committee (Sales *et al*., 2010). The approach was evaluated by comparing the segmentation result with a gold standard, obtained by manual segmentation drawn by an expert. The comparison is carried out by calculating the quality indices of segmentation proposed in Udupa *et al*. (2006), and compared the obtained result with those obtained by Unal *et al*. (2008).

The proposed technique to segment the media-adventitia borders is divided in three stages, pre-processing, processing, and post-processing, which have respectively several steps each, as summarized as follows:

Pre-processing

- Image size and resolution normalization;
- Transducer reflection attenuation;
- Speckle Filtering;
- Conversion to the polar domain.

Processing

- Feature extraction using DWPF;
- Binarization using Otsu;
- Morphological Combination.

Post-processing

- Branch-opening test and correction
- Return to the Cartesian domain;
- Adventitia-Contour extraction (Segmentation Concluded).

Pre-processing

Some IVUS-images characteristics could decrease the segmentation-process effectiveness. The pre-processing stage was created in order to attenuate the effects of those features, such as different image sizes, trans-

ducer reflection, speckle noise, and to convert the image into a more appropriated domain for processing.

Image size and resolution normalization – The importance of normalizing the image size and resolution is because they are dependent on the ultrasound transducer and equipment settings, and, as will be seen in the processing section, the morphological operation matrixes were created based on some vessel feature dimensions for a 400×400 pixel image with resolution of 25×25 μm² per pixel. Therefore, every image in the Cartesian domain was normalized to the mentioned size and resolution, so that the same matrix structure of the morphological operations could be used for any image.

Transducer reflection attenuation – The transducer reflection is characterized by a fixed and well known size and position. Considering the image size normalization, the distance between the image center to the innermost transducer reflection border is 40 pixels, followed by an width of 10 pixels. Therefore, everything inside a radius of 50 pixels is reflection, thus its attenuation could easily be made by reducing to zero the intensities of the referred pixels. However, in order to not create new undesirable borders in the images, the attenuation has to be linear and smooth through the reflection ring; therefore, for a 400×400 pixel image, the following linear equation is proposed:

$$I_{NoReflexion} = \begin{cases} \dfrac{I_{Original}}{10}, \text{ if } radius < 41 \text{ pixels} \\ \left(\dfrac{I_{Original}}{10}\right) \times (radius - 40), \text{ if } (41 \le radius < 51) \text{ pixels} \\ I_{Original}, \text{ otherwise} \end{cases} \quad (1)$$

where $I_{Original}$ are the pixels' intensities of the original image, $I_{NoReflexion}$ are the pixels' intensities of the image without the transducer reflection, the *radius* is the distance between the center of the image and current pixel.

Speckle filtering – The speckle noise contained in the image was filtered using the well-known Speckle Reducing Anisotropic Diffusion (SRAD) (Yu and Acton, 2002). This algorithm uses the concept of anisotropic diffusion for filtering the speckle without damaging the borders of the objects, as its predecessor (Perona and Malik, 1990), and also strengthens the borders. Depending on the kind of ultrasound images, the filter parameters have to be designed and optimized regarding some specific needs. In this case, the parameters were chosen focusing at the overall accuracy. Once, the first version of the algorithm was ready, we used 10 IVUS images to calibrate the parameters for the best segmentation result, which led to the following: Windows size in a homogenous region (40×40); Number of iterations n = 100 with Δt = 0.5 s.

Conversion to the polar domain (I_{Polar}) **–** Due to the fact that 1D appearance makes the computational processing simpler (Unal *et al*., 2008), the great majority of the operations were carried out in the polar domain (r, θ). Therefore, the conversion was performed from the Cartesian image at center (200,200) and size of 400×400 pixels to the polar domain one, resulting in a 200×630 pixel size image (Figure 1a).

Processing

The goal of this section is to get a binary image of the adventitia object in the polar domain. In order to achieve this goal, three known image processing techniques are combined: Wavelet, Otsu and Mathematical Morphology. The Wavelet and Otsu are used to extract from the pre-processed image as much vessels-feature information as possible; then, the Mathematical Morphology operations streamline this information, and estimate the missing one.

Feature extraction using DWPF – In order to be translating invariant, and able to model the decomposition tree, the Discrete Wavelet Packet Frame (DWPF) (Coifman and Wickerhauser, 1992; Katouzian *et al*., 2008a; 2008b) was used for extracting or highlighting the information from the pre-processed image (Figure 1b). The wavelet *Daubechie 1* (dB1) was chosen, by being symmetric, bi-orthogonal and compact, making the discrete analysis more practical (Misiti *et al*., 2000). After performing a first level decomposition using the binary tree structure (Mallat, 2009; Misiti *et al*., 2000) (Figure 1a), and disposing the coefficients as following (Stark, 2005):

$$\left(\begin{array}{c|c} cA1 & cD^h1 \\ \hline cD^v1 & cD^d1 \end{array}\right) \quad (2)$$

The coefficient of approximation ($cA1$) is the one that mostly extracts and highlights the desired information (Figure 1c).

Binarization using Otsu ($cA1_{bin}$) **–** One way to improve the feature extracted by the DWPF is using binary morphological operations. Therefore, the coefficients (Figure 2a) have to be binarized. Because single threshold would not yield the same result for every image, and the coefficient histograms are quite bimodals, we chose the threshold of every coefficient to be defined dynamically using Otsu (1979) for which one result can be seen in Figure 2b. It can be noted

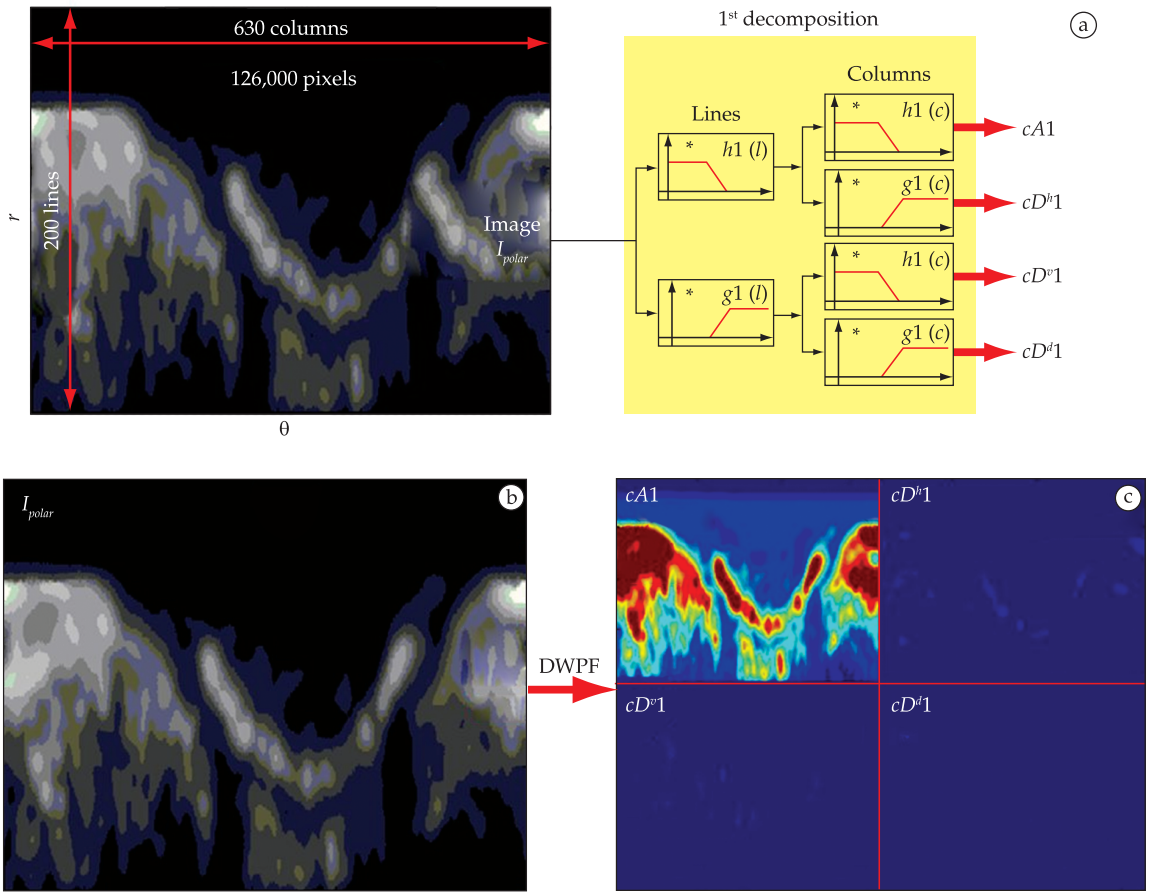

Figure 1. a) Example of the pre-processed image showing its size, and the one level decomposition tree for the DWPF. b) Pre-processed polar image. c) 1st decomposition coefficients of the DWPF.

that the coefficient of approximation binarized ($cA1_{bin}$) is also the one that provides more information regarding size and localization of the adventitia (Figure 2c in red), as well as plaques (Figure 2c in blue).

Morphological combination Adventitia Polar Object binary (APO_{bin}) – As mentioned in the previous section, the $cA1_{bin}$ is the binary image that has the highest plaque and adventitia information, which here will be called APO_{bin}. However, our goal is to get a binary image with the complete adventitia object. In order to achieve this goal, a combined set of mathematic-morphology operations (Gonzalez and Woods, 2008) is used, where the $cA1_{bin}$ is the root to generate three complementary images (Figure 3), which will be called Tissue Information (T_{inf}) (Figure 4), Adventitia Missing Region Information (A_{mis}) (Figure 5) and Skeleton (Skt) (Figure 6); these images are then combined, so that the adventitia information can be selected and processed to generate a binary image in the polar domain with the closest possible adventitia object (Figure 3).

The creation of the three complementary images, as well as the union, binary selection and polishing are explained below:

Complementary image 1 – Tissue Information: the T_{inf} (Figures 4b and 4d) is an image which brings information regarding the vessel wall internal border and the plaques, including the separation between them (elastic lamina). It is obtained by an opening operation (Gonzalez and Woods, 2008) between the $cA1_{bin}$ (Figures 4a and 4c) and a structuring element with 2 lines and 50 columns filled by ones ($S_{2\times50}$).

$$T_{inf} = cA1_{bin} \circ S_{2\times50} \quad (3)$$

The reason for this matrix dimension is to cut any connection between the plaques and adventitia which are usually smaller than 50 pixels in the angular direction (Figure 4c in yellow). By disconnecting them (Figure 4b and 4d), the plaques can be removed from the image by area selection, in later operations.

Complementary image 2 – Adventitia Missing Region Information: as the $cA1_{bin}$ do not give the com-

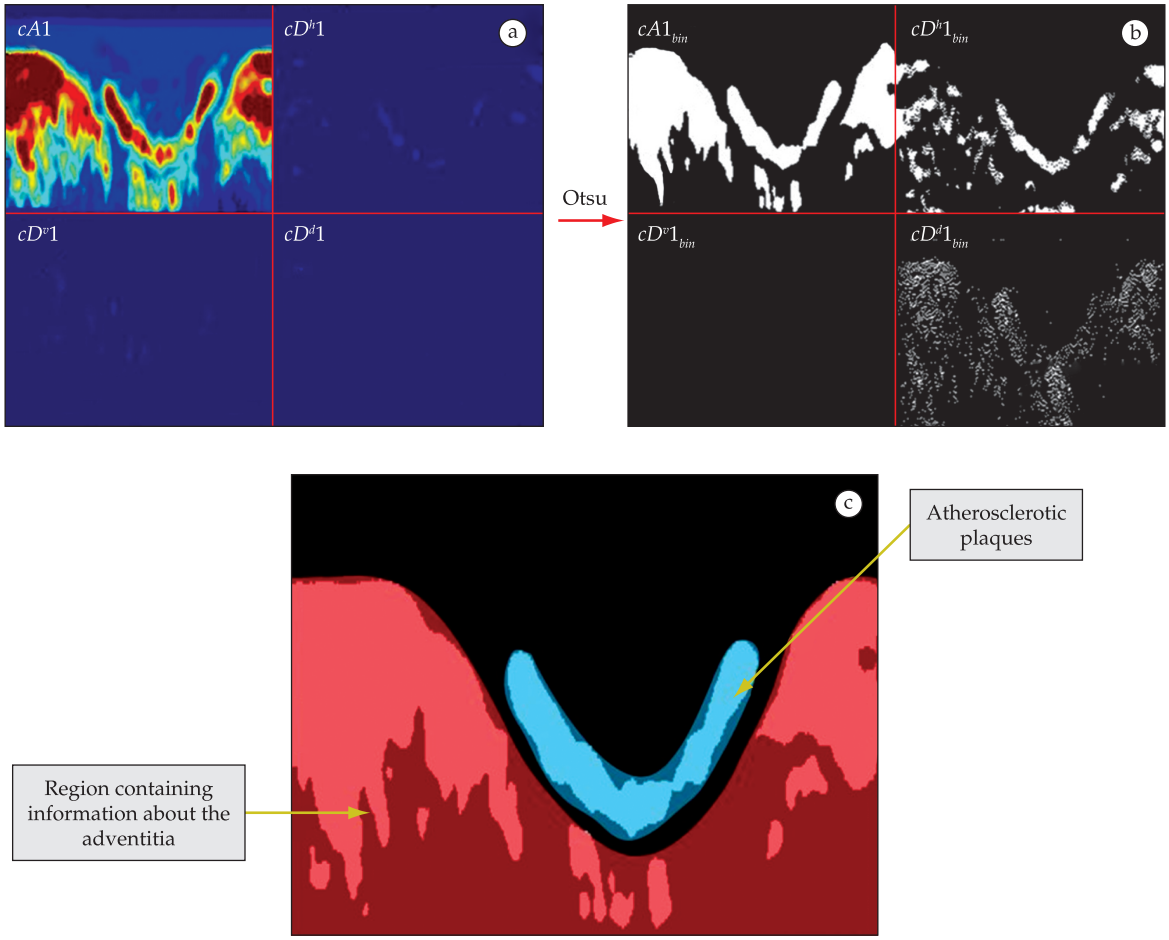

Figure 2. a) 1st decomposition coefficients of the DWPF. b) Coefficients binarized using Otsu method. c) Close look at the $cA1_{bin}$ coefficient, which contains the most relevant information regarding plaques and adventitia.

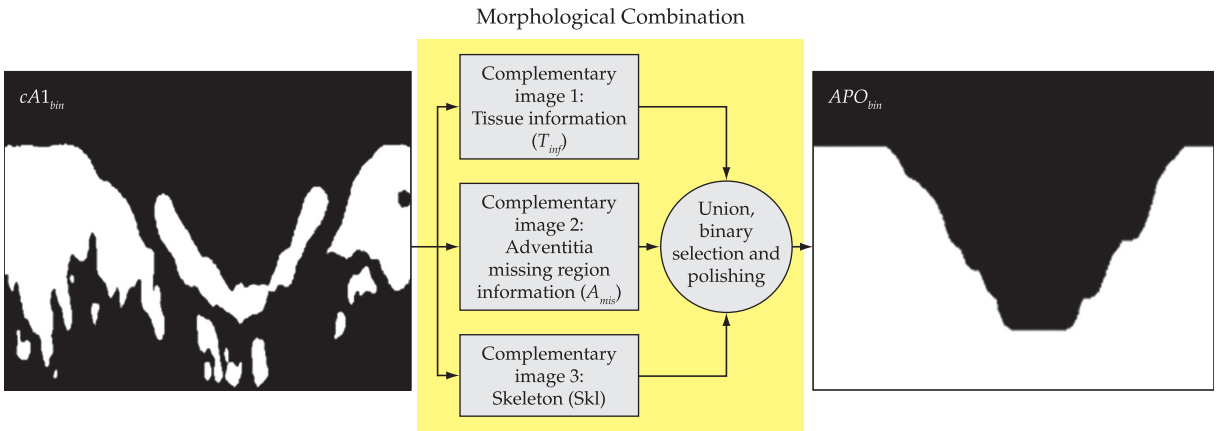

Figure 3. Morphological-combination diagram, created to obtain the binary Adventitia Polar Object (APO_{bin}) from the $cA1_{bin}$. The Adventitia Polar Object (APO_{bin}) is a binary image in the polar domain, with the adventitia shape and the plaque removed.

plete information regarding the adventitia region, as exemplified in Figure 5a in yellow, the missed region is estimated from the known information. This new image containing a prediction of what the adventitia would be in certain areas is called Adventitia Missing Region Information (A_{mis}) (Figure 5d). The prediction is made as follows: firstly, a thickening procedure (Gonzalez and Woods, 2008) is applied over $cA1_{bin}$.

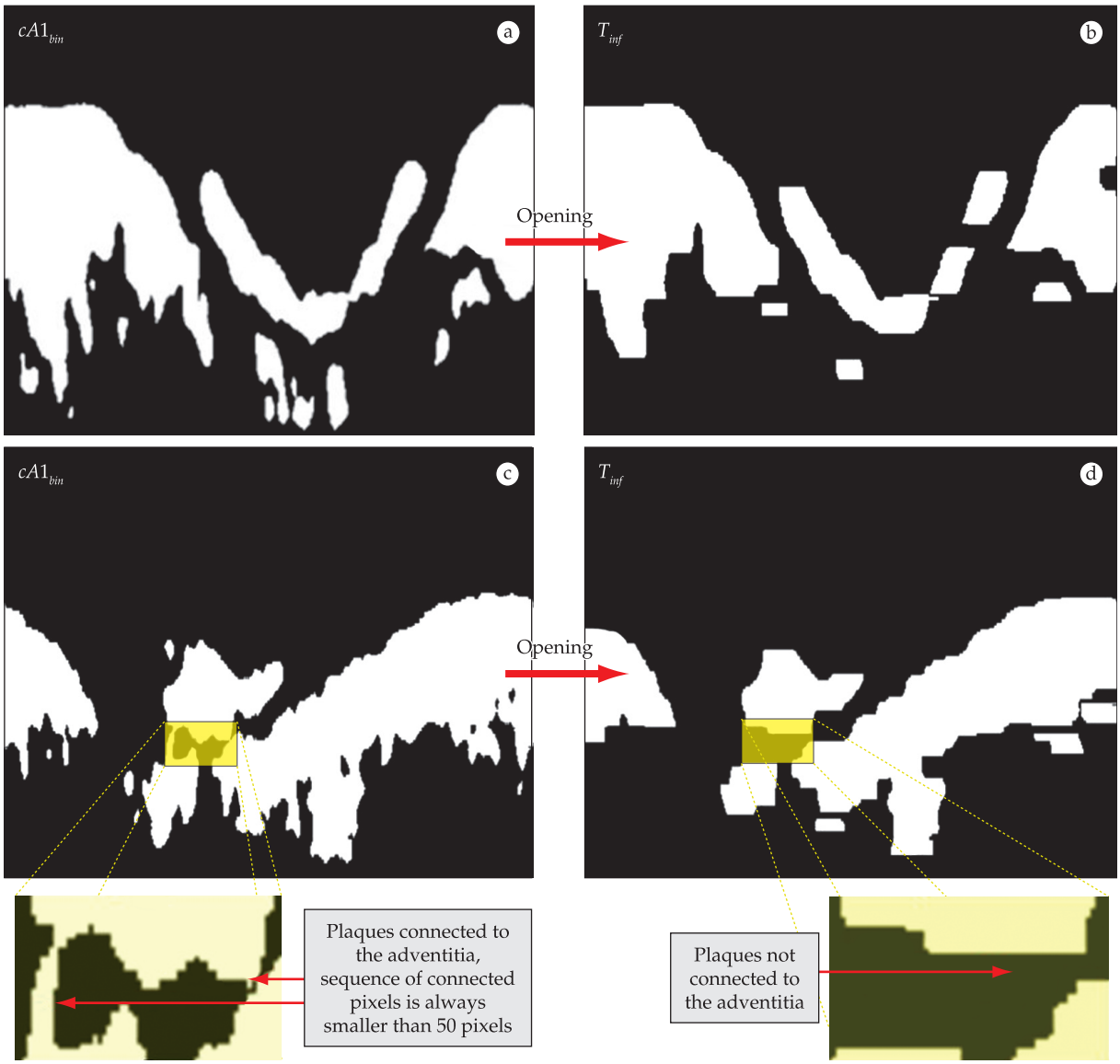

Figure 4. Demonstration of how to obtain the Tissue Information T_{inf} from $cA1_{bin}$ images, using an opening procedure. a) Example of $cA1_{bin}$ with no connection between the plaques and adventitia. b) Tissue Information T_{inf}, obtained by an opening operation at (a). c) Example of a $cA1_{bin}$ with connection between the plaques and adventitia. d) Tissue Information T_{inf}, obtained by an opening operation at (c), note that the connection was removed in order to separate the plaques from adventitia.

$$cA1_{binThik} = \left(\left(\ldots\left(\left(cA1_{bin} \wp S_R^1\right) \wp S_R^2\right)\ldots\right) \wp S_R^i\right) \quad (4)$$

where $\wp$ represents a thickening procedure, S_R^i is rotating structuring element (Gonzalez and Woods, 2008), where each 8 iteration (i = 1..8) the structuring element has one complete rotation, leading to 1 pixel thickening. Therefore, after 80 iterations, a thickening of 10 pixels is produced (Figure 5c), this number was chosen because it is the elastic-lamina average distance in this type of image (Figure 5b). By doing it, the plaque borders reach what would be the adventitia border (Figure 5c in red), and we have the closest prediction of the missing adventitia contour. Finally, the A_{mis} (Figure 5d) is obtained by an upward filling procedure at $cA1_{binThick}$ (Figure 5c yellow arrows), where its column is filled with ones upwardly, until it reaches the first white pixel.

$$A_{mis} = Fill_{upward}\left(cA1_{binThick}\right) \quad (5)$$

Complementary image 3 – Skeleton: if we unify the T_{inf} and A_{mis} (Figure 6a), complementary infor-

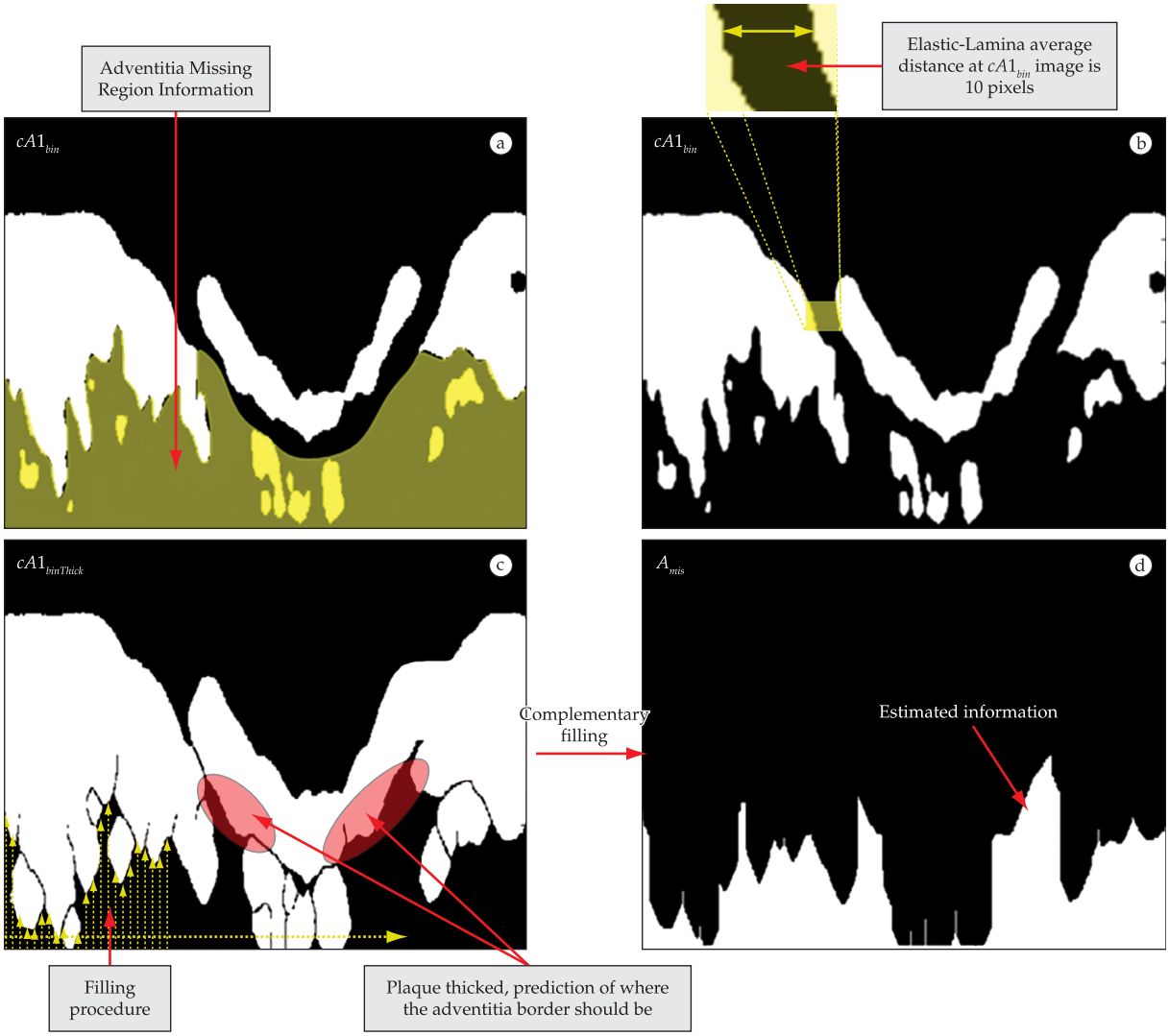

Figure 5. a) The $cA1_{bin}$ showing in yellow the adventitia missing information. b) The $cA1_{bin}$ exemplifying the elastic-lamina average size. c) The $cA1_{binThick}$, the result of a 10 pixel thickening procedure of $cA1_{bin}$. d) Estimated Adventitia Missing Region Information (A_{mis}).

mation about the plaques and vessels is made available. The goal now is to create a Skeleton (*Skt*) that could only connects the adventitia objects (Figure 6a in red), and thus separate them from the plaques (Figure 6a in blue) using binary area selection in the next stage. In order to create the *Skt* (Figure 6c), the $cA1_{bin}$ is closed, using a structuring element with 10 lines and 100 columns filled by ones ($S_{10\times100}$), followed by a downward filling procedure, generating a Closed and Filled downward Image (CF_{down}), where its column is filled with ones downwardly, from the first white pixel to the last column illustrated in red at Figure 6b.

$$CF_{down} = Fill_{down}\left(cA1_{bin} \bullet S_{10\times100}\right) \quad (6)$$

Afterwards, a Skeleton (Gonzalez and Woods, 2008) is carried out at CF_{down}, generating the *Skt* (Figure 6c)

$$Skt = \bigcup_{k=0}^{K} S_k\left(CF_{down}\right) \quad (7)$$

Note that the plaques are also considered in the CF_{down} (Figure 6b in red). However, after performing the skeleton, the *Skt* (Figure 6c) will only connect the adventitia objects, leaving the plaques to be removed.

Final polar domain image – Union, Binary Selection and Polishing: the complete adventitia shape in the polar domain (Figure 7c), is obtained as follows: firstly, the three complementary images (Figure 7a) are unified:

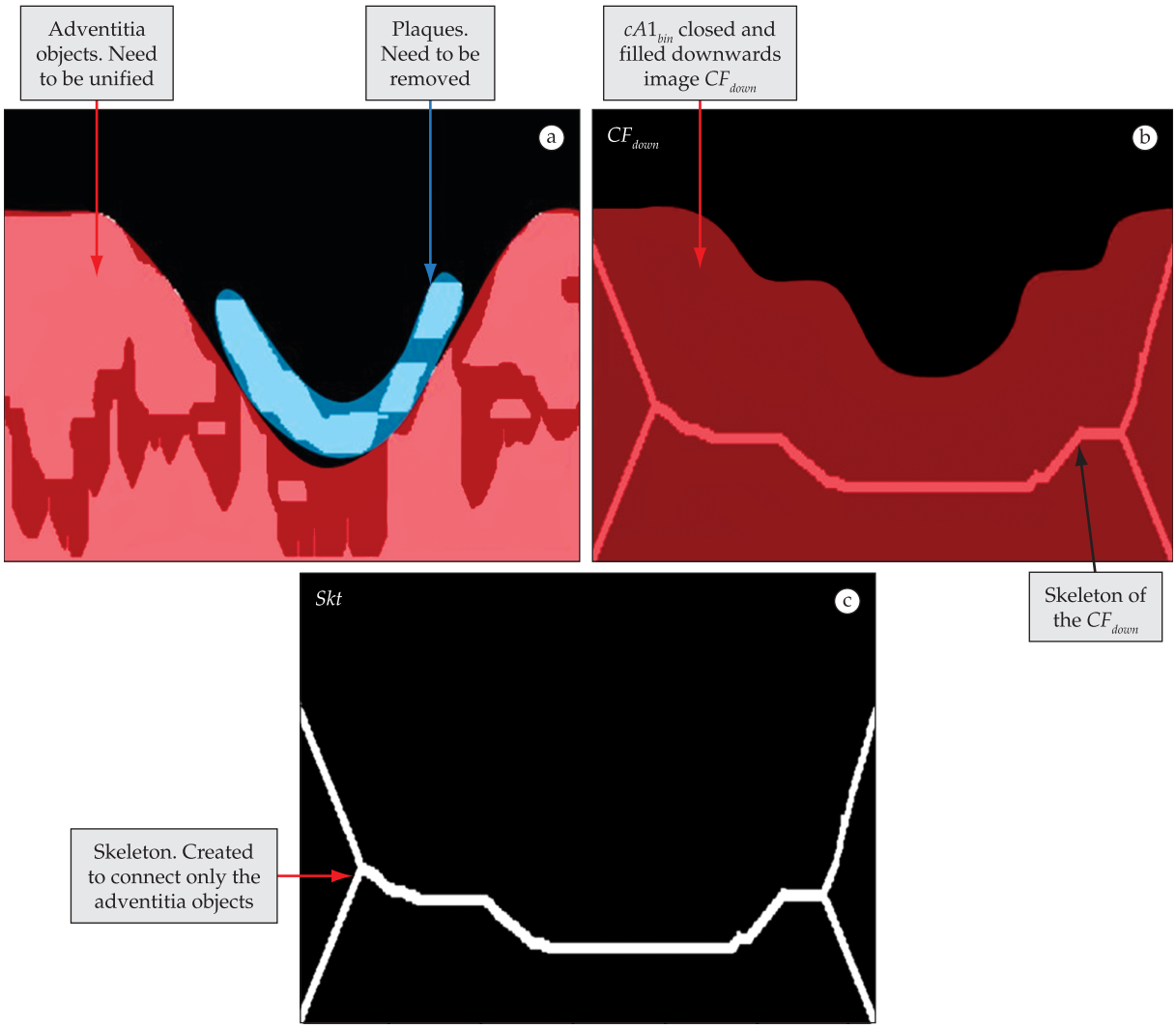

Figure 6. a) T_{inf} and A_{mis}, united, in red is the region that should be connected, in blue is the region that should be removed. b) In red (CF_{down}), is the $cA1_{bin}$ after a closing and filling procedure. In white, the Skeleton of CF_{down}. c) Skeleton, created to connect only the adventitia objects.

$$U = T_{inf} \bigcup A_{mis} \bigcup Skt \tag{8}$$

Secondly, the adventitia information is isolated, and the plaques are removed by processing a binary area selection, by processing a region growing procedure (Figure 7b) (Gonzalez and Woods, 2008). The region growing starting point is located in line 199 and column 2, position that will always be inside the Skeleton. Finally, a closing operation in the area selected, $B_{selected}$ (Figure 7b) will polish and result in an image with the adventitia information, called Adventitia Polished Object (APO_{bin}).

$$APO_{bin} = \left(B_{selected} \bullet S_{circular(50)}\right) \tag{9}$$

where the structuring element $S_{circular(50)}$ is a special matrix that disposes the ones in a circular way with 50 pixel diameter.

Post-processing

Test and correction of Side Branches – Side Branches are openings in some IVUS images, caused by vessel bifurcations where the transducer is acquiring the images. One of their features is the presence of huge gaps in the pre-segmented adventitia (Figure 8a). Therefore, it can be identified by taking and testing the derivative (Figure 8c) of a signal representing the column height of the polar image (Figure 8b):

$$h(\theta_i) = \sum_j APO_{bin}\left(r_j, \theta_i\right) \tag{10}$$

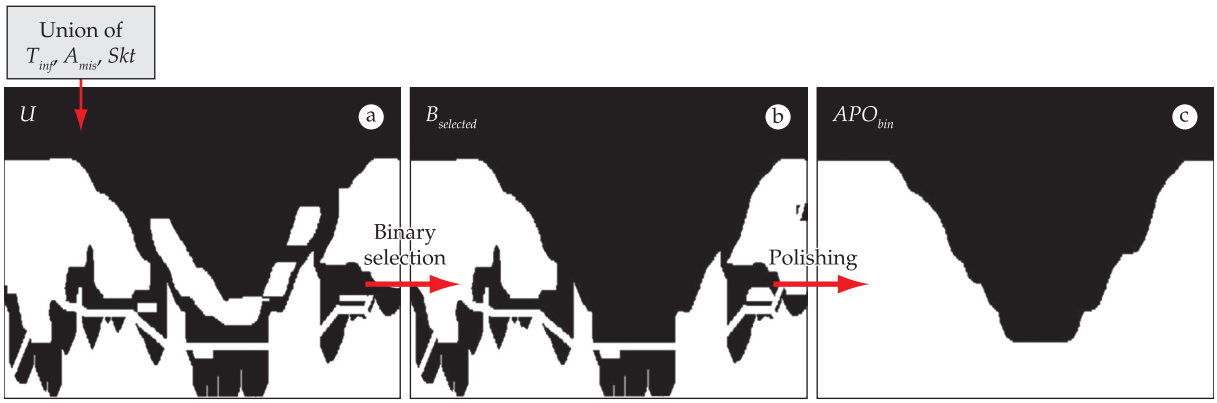

Figure 7. a) The 3 unified complementary image (T_{inf}, A_{mis}, Skt). b) Binary area selected, corresponding to adventitia. c) Image with the complete adventitia shape, after a closing procedure at (b).

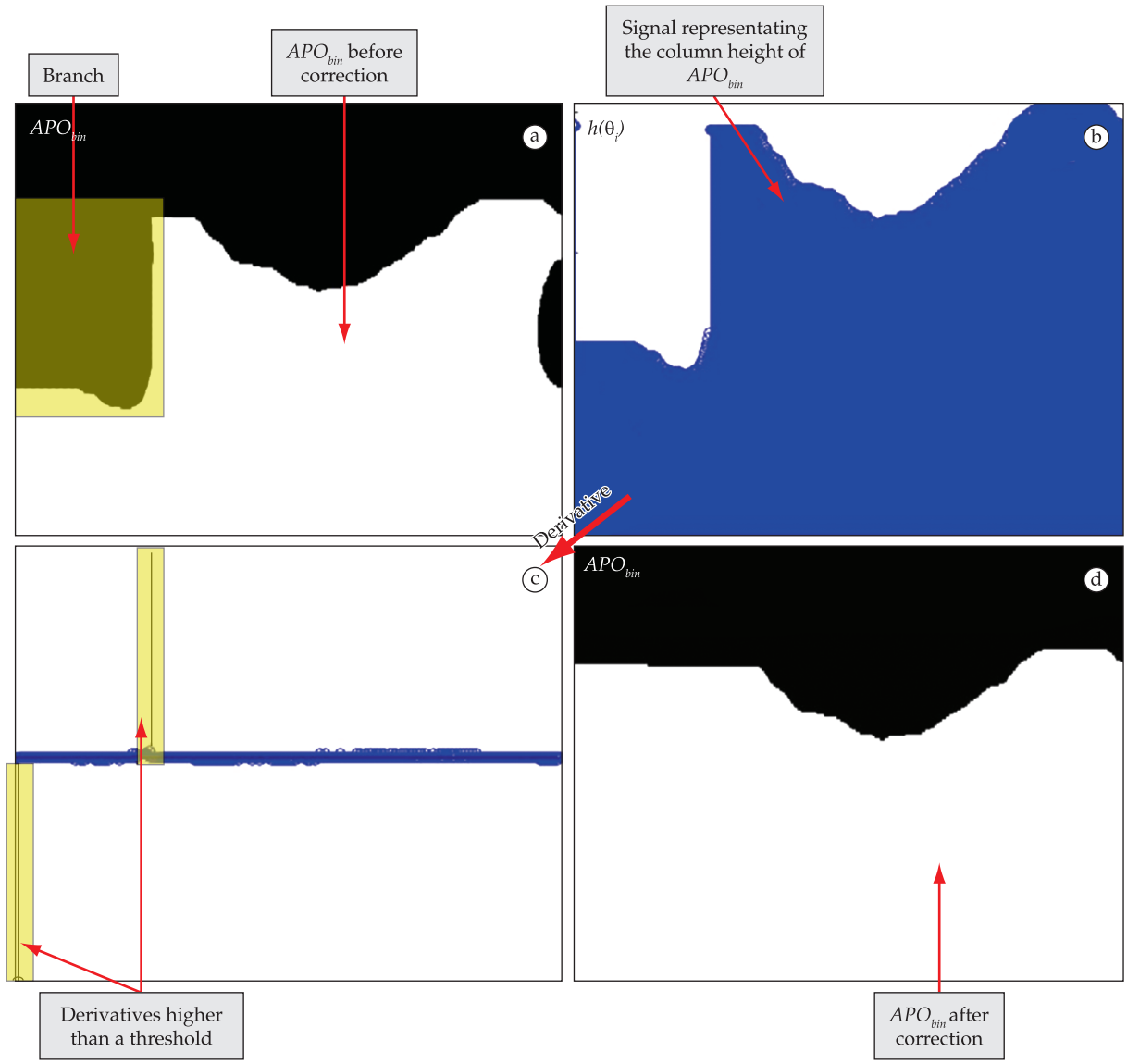

Figure 8. a) Adventitia Polar Object APO_{bin} with Branch. b) Signal representing the column height of the polar image $h(\theta_i)$. c) Derivative of $h(\theta_i)$. d) Corrected Adventitia Polar Object APO_{bin} image.

Given the 2 consecutive highest derivatives in modulus, the correction is performed by removing and interpolating (using Piecewise cubic Hermite) the values corresponding to the gap; the interpolated signal is then returned to the polar image and the correction is finished (Figure 8d).

Returning to the cartesian domain – After the Side Branch detector, the binary polar image is then returned to the Cartesian domain, and its logical negation is performed (Figure 9a).

Adventitia contour extraction – The contour is extracting from the Cartesian domain image using:

$$\beta(I_{Cartesian}) = I_{Cartesian} - (I_{Cartesian} \varepsilon S_{3x3}) \quad (11)$$

where ε represents an erosion procedure and $S_{3\times3}$ is a structuring element with 3 lines and 3 columns filled by ones. The segmentation is concluded by placing this contour on the original image, generating I_{Final} (Figure 9b).

$$I_{Final} = \beta(I_{Cartesian}) \cup I_{Original} \quad (12)$$

Results and Evaluation

In order to evaluate our approach, 100 IVUS images from 24 patients obtained from the data base of the Heart Institute of São Paulo, Brazil (InCor) were segmented. There were images with and without branches, different vessel sizes, and 88% of the images contained calcified, fibrotic and lipid plaques. The computational cost was processing from an Intel Core 2 Duo, 2.53 GHz, 4 GB of RAM, Windows Vista 32 bits and MATLAB® 2009a. The average segmentation time for the 100 images was (4.82 ± 0.24) s. The segmentation quality was measured by comparing each individual result (Figures 10a, c, e and g) with their manual segmentation (respectively Figures 10b, d, f and h), made by an expert (gold standard), according to part of the evaluation method presented by Udupa *et al*. (2006). Specifically, the proportion of True Positive (TP), False Positive (FP), False Negative (FN), and also the Maximum Positive Deviation (Max_{FP}) and Maximum Negative Deviation (Max_{FN}) were computed. As can be seen in Table 1, the considerably high method's accuracy is demonstrated not only by the TP and FP good performance, in which the agreement were marginally smaller than 93% and close to 3% respectively, but also the Max_{FP} and Max_{FN} insignificant distance values, respectively lower and higher than 0.3 mm (considering the image dimensions of 10×10 mm). In addition, the small and consistent standard deviation among the related parameters show the algorithm's high precision.

So as to validate and reinforce our outcome quality, we compared it to a recent one in the literature (Unal *et al*., 2008). However, the parameters used to measure their effectiveness (Unal *et al*., 2008) were also adopted: Overlap Ratio (OR) [OR=TP/(TP+FN+FP)]; False Positive Rate (FPR) [FPR=FP/(FP+TN)]; False Negative Rate (FNR) [FNR=FN/(FN+TP)], as well as the Maximum Distance ($Max_{DISTANCE}$) [$Max_{DISTANCE}$ = max (Max_{FP}, Max_{FN})]. FPR will not be considered here, since it uses True Negative (TN) which is very sensitive to the image size and resolu-

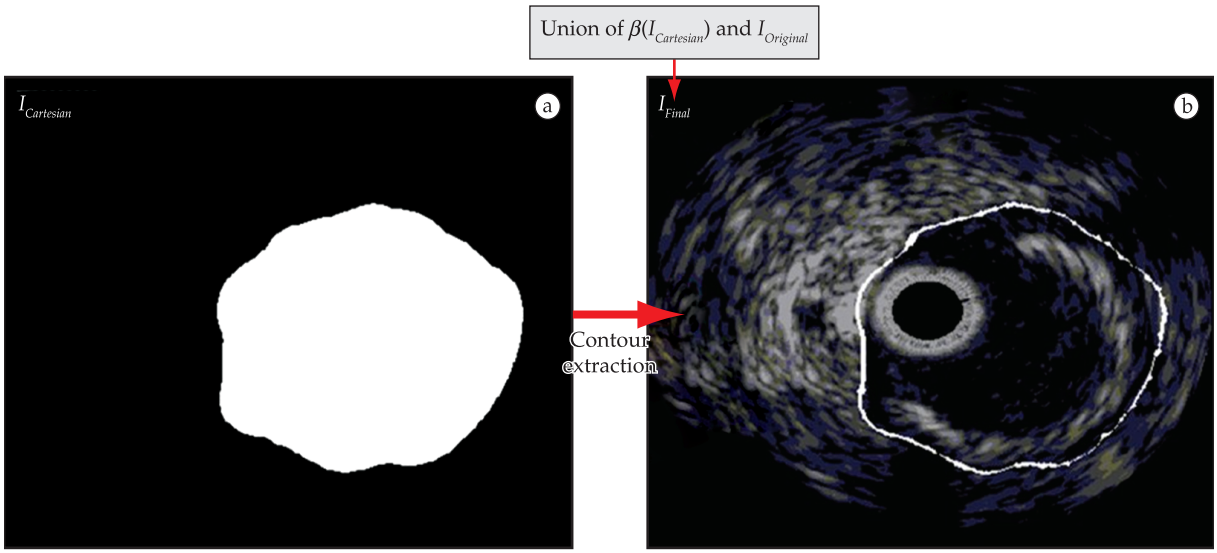

Figure 9. a) Image in the Cartesian domain $I_{Cartesian}$. b) Final image I_{Final}, image segmented, after extracting the contour.

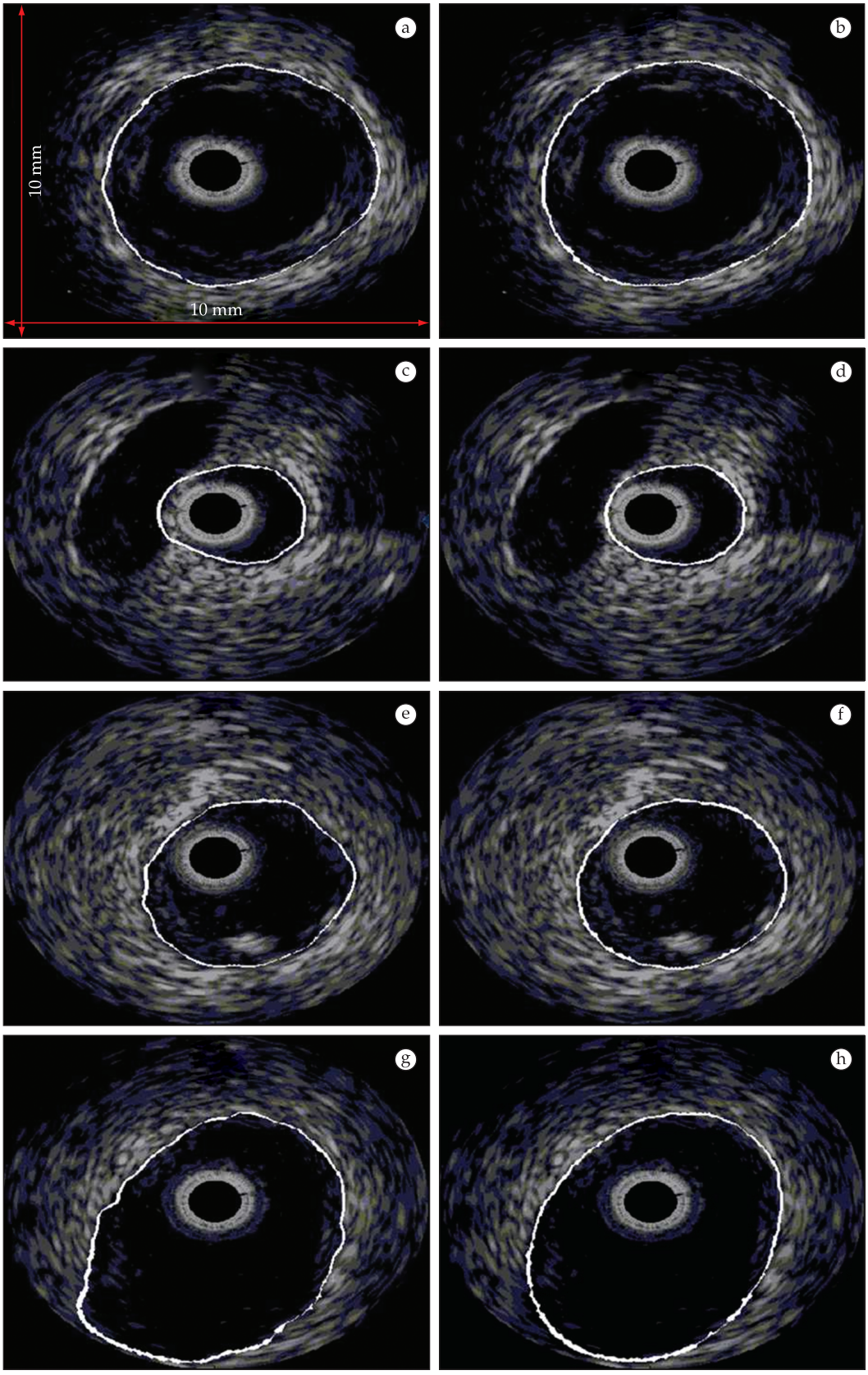

Figure 10. a), c), e) and g) are some of IVUS-image segmentation examples made by this automated method. Respectively b), d), f) and h) are their corresponding images segmented by an expert used as gold standards.

tion. As mentioned in the section **The state of the art**, Unal *et al*. (2008) obtained 2 different results, which correspond to two groups of images. The first one (Unal Method 1) uses a set of images with only small calcification and branch opening, no feature detection is tested. The second (Unal Method 2), also uses the first set of images including others with large size calcification and branch openings. Table 2 depicts a comparison of these 3 parameters, the two results obtained by Unal *et al*. (2008) and the correspondent values of this approach. The outcome differences will be explained with more detail in the **Discussion and Conclusion** section. Nevertheless, as expected, the values showed to some extent a consistence with relatively small difference between corresponding parameters, and somewhat reinforce the segmentation quality.

Discussion and Conclusion

A new segmentation technique is presented; it combines some well known image processing techniques aiming at segmenting the adventitia in IVUS images with higher accuracy. As presented in the **Results and Evaluation** section, the visual results (Figure 10) and the first statistical results (Table 1), using the parameters proposed by Udupa *et al*. (2006), proved this approach effectiveness. Nonetheless, in order to demonstrate the outcome quality we also computed other index to compare to a recent and established work (Table 2). The first result in Table 2 (Unal Method 1) has the highest accuracy. However, in this test, they used a set of images with minor calcification and branch opening; in other words, images considered easy to segment. For the second result in Table 2 (Unal Method 2), they used the first set of images, adding to them some more challenging ones, with large calcification and branch opening. In total, they used 66% of images from the first set and 34% of challenging images. Due to this addition, the second test had degradation in its result (Table 2). In our test, we tried to build a medium-sized, but challenging and balanced dataset, balanced in a sense of having a variety of images with different kinds of features, such as different lumen and adventitia size, containing different concentration and size of the 3 plaques, and with branch opening. We cannot state which dataset is harder to segment, but due to the high percentage of challenging images, the equivalent result of our approach could be fairly compared to the (Unal Method 2). The difference between the result of our approach and theirs, at the OR(%) and FNR(%), respectively, are less than 1% and 2% each, which can be easily compensated by our lower standard deviation and $Max_{DISTANCE}$ (mm) (Table 2). Therefore, considering the different level of difficulties between datasets, the minimum difference at the concerning parameters (OR, FNR and $Max_{DISTANCE}$ (mm)), and the smaller standard deviation of the proposed approach, the results can be said to be very similar. Nonetheless, the proposed approach is much simpler; it does not need to process well known timing consuming tasks, such as computation of large covariance, estimation of PDFs and going through an energy minimization process as in Unal *et al*. (2008), as well as not having to convert the image into vector and returning some indexed vector after a k-means clustering as in Katouzian *et al*. (2008b).

To conclude, the association of the image processing techniques led to a very good result, encouraging its use. The main contributions of this work are: a) a simple but effective way of extracting the catheter reflection, without creating new borders; b) a combination of imaging processing techniques (SRAD, DWPF, Otsu), as well as their optimum parameters, number of iterations, which led to an image with a large amount of information about the tissue and plaques; c) sequence of well designed morphologi-

Table 1. Assessment of the proposed approach for 100 images using the index suggested by Udupa *et al*. (2006).

Index used by	Parameters				
Udupa *et al*. (2006)	TP (%)	FP (%)	FN (%)	Max_{FP} (mm)	Max_{FN} (mm)
Proposed Approach	92.83 ± 4.91	3.43 ± 3.47	7.17 ± 4.91	0.27 ± 0.22	0.31 ± 0.2

Table 2. Result comparison among the methods and parameters of three different datasets using the index suggested by Unal *et al*. (2008).

Index used by	Parameters		
Unal *et al*. (2008)	OR (%)	FNR (%)	$Max_{DISTANCE}$ (mm)
Unal Method 1	92.23 ± 6.27	5.35 ± 7.86	0.84 ± 1.74
Unal Method 2	90.57 ± 10.66	5.55 ± 9.20	0.98 ± 1.78
Proposed Approach	89.79 ± 4.51	7.17 ± 4.91	0.31 ± 0.2

cal operations to isolate the adventitia with good results; d) segmentation results of challenging images, to be analyzed and compared with new approaches in the future. Certainly, the association of different operators and settings would change the results and the segmentation goal, leaving room for new studies and tests. Therefore future works should investigate new parameters and settings to perform the lumen segmentation. Adding to that, the other methods (Katouzian *et al*., 2008b; Unal *et al*., 2008) will be implemented, and by using the same dataset and computer, a detailed comparison of the segmentation quality and computational cost, among the three segmentation methods could be discussed.

Acknowledgements

For the financial and material support, we would like to thank CNPq (National Council of Scientific and Technological Development - Brazil), InCor (Heart Institute of São Paulo, Brazil), LEB-USP (Biomedical Engineering Laboratory of the State University of São Paulo). We also would like to thank all the reviewers, the editor and the unknown referees, who have given immeasurable contributions to this work.

References

BARAJAS, J.; CABALLERO, K. L.; RODRIGUES, O.; RADEVA, P. Cardiac phase extraction in IVUS sequences using 1-D Gabor filters. In: ANNUAL INTERNATIONAL CONFERENCE OF THE IEEE, 29. 2007, Lyon. **Proceedings**… EMBS, 2007. p. 343-346.

CHAN, F.; VESE, L. A. Active contours without edges. **IEEE Transactions on Image Processing**, v. 10, n. 2, p. 266-277, 2001.

COIFMAN, R. R.; WICKERHAUSER, M. V. Entropy-based algorithms for best basis selection. **IEEE Transaction on Information Theory**, v. 38, n. 2, p. 713-718, 1992.

DAWANT, B. M.; ZIJDENBOS, A. P. Image Segmentation. In: FITZPATRICK, J. M.; SONKA, M. (Eds.). **Handbook of medical imaging**: medical image processing and analysis. v. 2. Bellingham: SPIE Press, 2000. p. 71-128.

GONZALEZ, R. C.; WOODS, R. E. Morphological image processing. In: _____. **Digital image processing**. 3rd ed. New Jersey: Pearson Prentice Hall, 2008. p. 627-688.

KATOUZIAN, A.; BASERI, B.; KONOFAGOU, E. E.; LAINE, A. F. Texture-driven coronary artery plaque characterization using wavelet packet signatures. In: IEEE INTERNATIONAL SYMPOSIUM ON BIOMEDICAL IMAGING: FROM NANO TO MACRO, 5. 2008, Paris, **Proceedings**… IEEE, 2008a. p. 197-200.

KATOUZIAN, A.; BASERI, B.; KONOFAGOU, E. E.; LAINE, A. F. Automatic detection of blood versus non-blood regions on intravascular ultrasound (IVUS) images using wavelet packet signatures. In: MEDICAL IMAGING 2008: ULTRASONIC IMAGING AND SIGNAL PROCESSING, 2008, San Diego. **Proceedings**… SPIE, 2008b. p. 69200H.

LOBREGT, S.; VIERGEVER, M. A. A discrete dynamic contour model. **IEEE Transactions on Medical Imaging**, v. 14, n. 1, p. 12-24, 1995.

MALLAT, S. Wavelet Packet and Local Cosine Bases. In: _____. **A wavelet tour of signal processing**: the Sparse Way. 3rd ed. Burlington: Academic Press, 2009. p. 377-432.

MAURICE, R. L.; OHAYON, J.; FINET, G.; CLOUTIER, G. Adapting the Lagrangian speckle model estimator for endovascular elastography: theory and validation with simulated radio-frequency data. **Journal of Acoustic Society of America**, v. 116, n. 2, p. 1276-1286, 2004.

MISITI, M.; MISITI, Y.; OPPENHEIM, G.; POGGI, J. M. Wavelets: a new tool for signal analysis. In: _____. **Wavelet toolbox user's guide version 2**. Natick: The Math Work Inc., 2000. p. 3-37.

NYÚL, A. L. G.; FALCÃO, A. X.; UDUPA, J. K. Fuzzy-connected 3D image segmentation at interactive speeds. **Elsevier on Graphical Models**, v. 64, p. 259-281, 2003.

OTSU, N. Threshold selection method from gray-level histograms. **IEEE Transactions on Systems, Man and Cybernetics**, v. 9, n. 1, p. 62-66, 1979.

PEDNEKAR, A. S.; KAKADIARIS, I. A. Image segmentation based on fuzzy connectedness using dynamic weights. **IEEE Transactions on Image Processing**, v. 15, n. 6, p. 1555-1562, 2006.

PERONA, P.; MALIK, J. Scale-space and edge detection using anisotropic diffusion. **IEEE Transaction on Pattern Analysis and Machine Intelligence**, v. 12, n. 7, p. 629-639, 1990.

REIBER, J. H. C.; KONING, G.; DIJKSTRA, J.; WAHLE, A.; GOEDHART, B.; SHEEHAN, F. H.; SONKA, M. Angiography and intravascular ultrasound. In: FITZPATRICK, J. M.; SONKA, M. (Ed.). **Handbook of medical imaging**: medical image processing and analysis. v. 2. Bellingham: SPIE Press, 2000. p. 711-808.

SALES, F. J.; FALCÃO, B. A.; FALCÃO, J. L.; RIBEIRO, E. E.; PERIN, M. A.; HORTA, P. E.; SPADARO, A. G.; AMBROSE, J. A.; MARTINEZ, E. E.; FURUIE, S. S.; LEMOS, P. A. Evaluation of plaque composition by intravascular ultrasound "virtual histology": the impact of dense calcium on the measurement of necrotic tissue. **EuroIntervention** , v. 6, n. 3, p. 394-399, 2010.

STARK, H. G. The discrete wavelet transform. In: _____. **Wavelets and signal processing**: an application-based introduction. New York: Springer-Verlag, 2005. p. 43-91.

UDUPA, J. K.; LEBLANC, V. R.; ZHUGE, Y.; IMIELINSKA, C.; SCHMIDT, H.; CURRIE, L. M.; HIRSCH, B. E; WOODBURN, J. A framework for evaluating image segmentation algorithms. **Computerized Medical Imaging and Graphics**, v. 30, n. 2, p. 75-87, 2006.

UDUPA, J. K.; SAMARASEKERA, S. Fuzzy connectedness and object definition: theory, algorithms, and applications in image segmentation. **Graphical Models and Image Processing**, v. 58, n. 3, p. 246-261, 1996.

UNAL, G.; BUCHER, S.; CARLIER, S.; SLABAUGH, G.; FANG, T.; TANAKA, K. Shape-Driven Segmentation of the Arterial Wall in Intravascular Ultrasound Images. **IEEE Transactions on Information Technology in Biomedicine**, v. 12, n. 3, p. 335-347, 2008.

XU, C.; PHAM, D. L.; PRINCE, J. L. Image segmentation using deformable models. In: FITZPATRICK, J. M.; SONKA, M. (Ed.). **Handbook of medical imaging**: medical image processing and analysis. v. 2. Bellingham: SPIE Press, 2000. p. 129-174.

XU, C.; PRINCE, J. L. Snakes, shapes, and gradient vector flow. **IEEE Transactions on Image Processing**, v. 7, n. 3, p. 359-369, 1998.

YU, Y.; ACTON, S. T. Speckle reducing anisotropic diffusion. **IEEE Transactions on Image Processing**, v. 11, n. 11, p. 1260-1270, 2002.